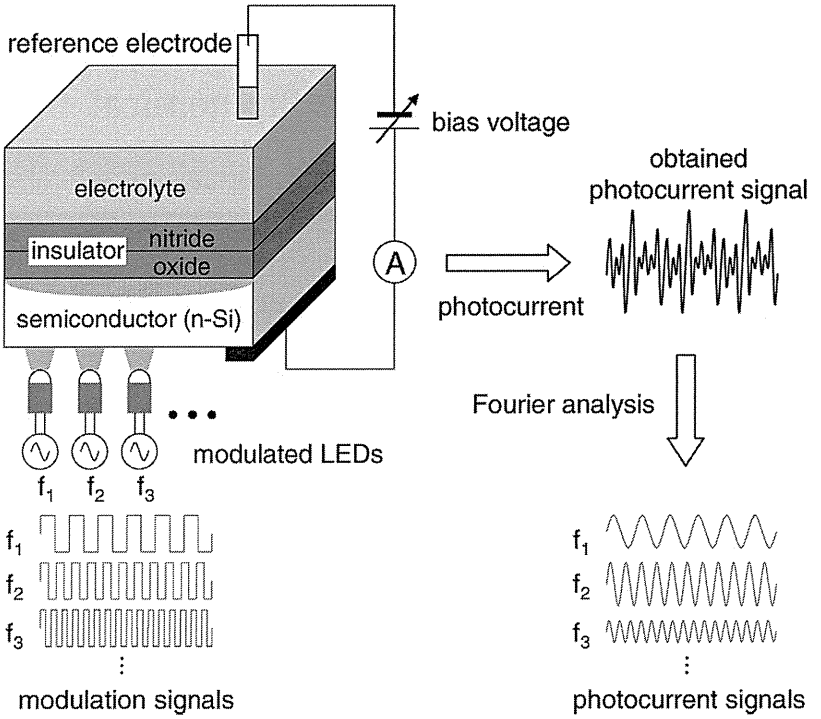

Fig. 1. Diagram of simultaneous measurement at multiple points on the sensing surface by frequency division multiplex.

in which the front-side or the back-side surface of the sensor plate is illuminated, respectively, by the modulated light. In the case of back-side illumination, which is the geometry of conventional LAPS measurement, the modulation frequency is limited by the low-pass filtering characteristics of carrier diffusion across the sensor plate. In front-side illumination, on the other hand, higher frequencies can be used, because photocarriers are directly generated and separated inside the depletion layer and no diffusion process is involved [8]. Front-side illumination, however, has some restrictions. For front-side illumination, the modulated light beam has to transit through the object to be measured. The object, therefore, must be light-transmissive and the distribution of the light transmittance of the object must be invariant while the pH distribution changes.

In this study, we developed a high-speed chemical imaging system based on the combination of FDM, a two-dimensional array of LEDs and front-side illumination. Front-side illumination allowed a wide bandwidth of the modulation frequency required for high-speed measurement by FDM. The developed system achieved high-speed chemical imaging at about 70 fps and provided real-time observation of a spatiotemporal change of pH distribution in a solution.

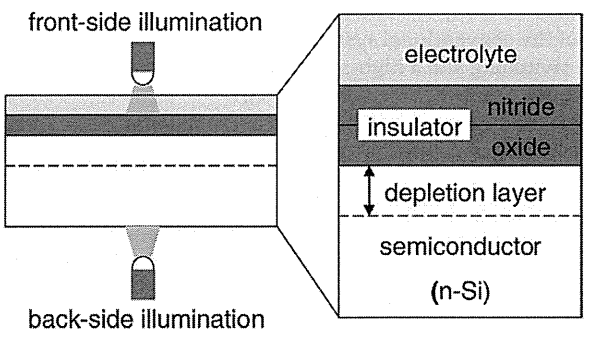

Fig. 2. Two different geometries of the LAPS measurement: front-side and back-side illuminations.

2. Experimental

Fig. 3(a) shows a schematic view of the high-speed chemical imaging system developed in this study. This system consists of a sensor plate, a two-dimensional array of LEDs (LED matrix), an oscillator array and a control PC with measurement software.

2.1. Sensor plate

The sensor plate (36 mm × 36 mm) used in this study was made of n-type Si wafer with a thickness of 200 μm and a resistivity of 10–20 Ω cm. The top surface of the sensor plate was covered with a 50 nm-thick thermal SiO_2 layer to obtain a semiconductor–insulator interface with low trap density and subsequently a 100 nm-thick Si_3N_4 layer deposited by low-pressure chemical vapor deposition (LP-CVD). The surface of the Si_3N_4 layer functions as a pH-sensitive surface when brought into contact with the sample solution. A thin ohmic electrode was deposited on the back-side of the sensor plate.

2.2. LED matrix

Fig. 3(b) shows the top view of the LED matrix with 7 × 5 LEDs (TA07-11SRWA, Kingbright Elec. Co., Ltd.) installed above the sensor plate as a light source. The peak wavelength and the intensity of illumination are 660 nm and 24 mcd, respectively. The light-emitting face of the LED matrix is immersed directly into the sample solution. The distance between the LED matrix and the sensor surface, or the thickness of the solution layer, through which the light has to pass, is about 0.6 mm. Five different frequencies are input to each column of the LED matrix and five points on the sensor surface corresponding to the five LEDs on one line are measured in parallel. By electrically switching the illuminating lines from the first to the seventh row in sequence, ion concentration values at all 35 points are obtained without mechanical scan.

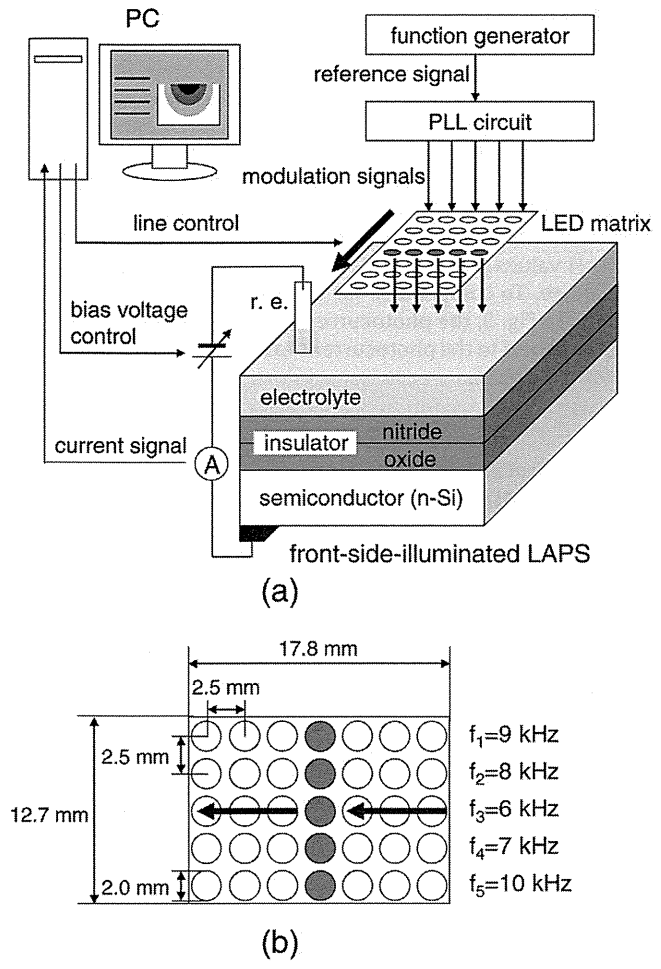

Fig. 3. (a) Schematic view of the high-speed chemical imaging system based on front-side-illuminated LAPS, and (b) top view of the LED matrix used in this system.

2.3. Oscillator array

Five modulation frequency signals of 6, 7, 8, 9 and 10 kHz are generated as integer multiples of the reference frequency of 100 Hz by a 5-channel phase-locked loop (PLL) synthesizer.

2.4. PC and software

A software developed with LabVIEW (National Instruments Corp.) is used to control the bias voltage between the reference electrode and the sensor plate, to switch a line of the LED matrix in sequence, to measure the photocurrent, to calculate each frequency component by the method described in our previous paper [4] and to display the obtained chemical image.

3. Results and discussion

3.1. Front-side vs. back-side illumination

To compare the performance of front-side and back-side illuminations, I–V curves were measured in both geometries at various frequencies in the range of 5–110 kHz. The test solution was a pH 7 buffer solution, and the sampling frequency and the sampling time were 500 kHz and 20 msec, respectively. The bias voltage was swept from −2.0 to 0.0 V at a step of 10 mV.

Fig. 4(a) compares the I–V curves obtained with front-side and back-side illuminations, respectively, at a modulation frequency of

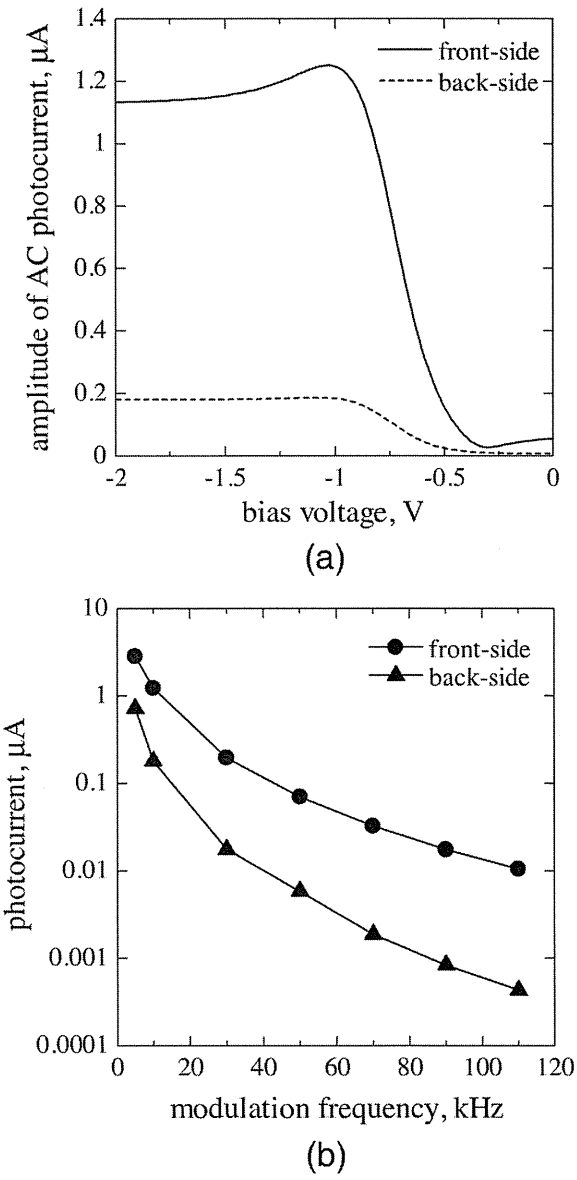

Fig. 4. (a) I–V curves for front-side or back-side illumination in the case of LED light modulated at 10 kHz, and (b) magnitudes of photocurrent as a function of the modulation frequency for front-side and back-side illuminations.

10 kHz. In the case of back-side illumination, electron–hole pairs are generated near the back-side surface of the Si substrate and the photocarriers reach the depletion layer by diffusion. While only those photocarriers separated in the depletion layer contribute to the external photocurrent, a large part of generated photocarriers are lost by recombination during the diffusion process, and the obtained photocurrent becomes small. In the case of front-side illumination, on the other hand, the electron–hole pairs are generated and separated directly in the depletion layer, and therefore, a larger photocurrent is obtained [8].

Fig. 4(b) shows the magnitude of photocurrent as a function of the modulation frequency for front-side and back-side illuminations, where the magnitude was defined as the difference of the maximum and minimum values of photocurrent in the I–V curve. Although the photocurrent decreases with the modulation frequency in both geometries, the decrease in back-side illumination is steeper than that in front-side illumination, which can be explained in terms of the low-pass filtering effect of carrier diffusion in the semiconductor layer.

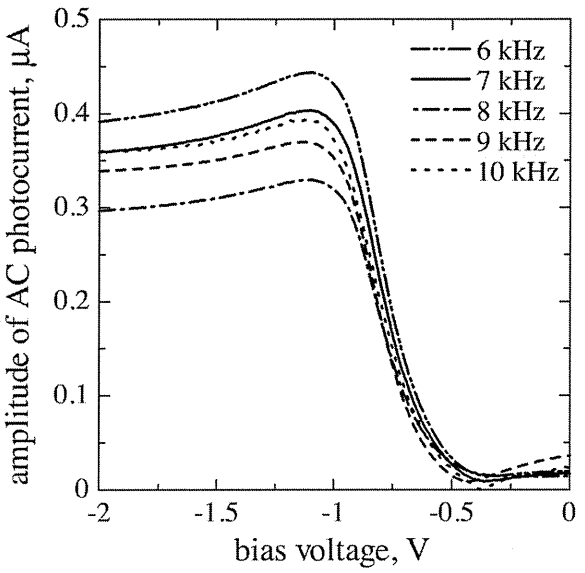

Fig. 5. I–V curves for simultaneous measurement by frequency division multiplex on one line of the LED matrix with 5 LEDs modulated at 6, 7, 8, 9 and 10 kHz.

These results demonstrate that front-side illumination, which offers a wider bandwidth of the modulation frequency, is more suitable for high-speed chemical imaging.

3.2. Parallel measurement

As a test of parallel measurement with FDM, five I–V curves were simultaneously obtained with five LEDs on the fourth row of the LED matrix modulated at different frequencies of 6, 7, 8, 9 and 10 kHz. The test solution was again a pH 7 buffer solution, the sampling frequency and sampling time were 200 kHz and 50 ms, and the bias voltage was swept from −2.0 to 0.0 V with a step of 10 mV.

Fig. 5 shows the amplitudes of the photocurrent of each frequency component as functions of the bias voltage. It was demonstrated that five I–V curves at different positions on the sensing surface could be simultaneously obtained. As observed in Fig. 5, however, the heights of I–V curves may differ due to the frequency-dependence of the photocurrent, variation of light intensities among LEDs and non-uniformity of the sensor plate. Therefore, it is necessary to normalize the measured photocurrent at each pixel to compensate for such artifacts.

3.3. Chemical imaging

In a LAPS measurement, the ion concentration in the sample solution is calculated from the shift of the I–V curve along the voltage axis. In chemical imaging, however, measurement of I–V curves at all pixels would be too time-consuming, and therefore, the photocurrent under a constant bias voltage is recoded at each pixel and converted into the ion concentration values. In the case of a sensor plate with n-type semiconductor, the photocurrent decreases for lower pH values and increases for higher pH values under a fixed bias voltage. To compensate for the variation of photocurrent as was seen in Fig. 5, the photocurrent value measured at each pixel was normalized to the photocurrent value measured in advance for a uniform solution.

3.3.1. Chemical imaging of pH buffer solutions

As a test of pH imaging, chemical images of a series of buffer solutions of pH 4–10 (Titrisol®, Merck KGaA, Germany) were acquired. The photocurrent value at each pixel was normalized to the photocurrent values of uniform pH 7 buffer solution. Fig. 6 shows a series of chemical images for pH 4–10 buffer solutions. As shown in Fig. 6, these chemical images are almost uniform in color representations corresponding to the uniformity of buffer solutions. Fig. 7 shows the average of the normalized photocurrent over all 35 pixels as a function of the pH value. A linear dependence of the normalized photocurrent on the pH value was observed with a slope of about 0.26/pH. This experimental result indicates that the developed system is capable of imaging pH values in the range of pH 4–10.

3.3.2. High-speed chemical imaging of pH change

Using the developed chemical imaging system based on front-side-illuminated LAPS, a high-speed chemical imaging experiment was performed to observe the spatiotemporal changes of pH values caused by injection of acid into a solution. The sampling frequency and the sampling time per line were 400 kHz and 10 ms. It takes, therefore, 70 ms to scan a frame of 7 lines, which corresponds to a frame rate of about 14 fps.

Fig. 8(a) shows the snapshots of 14 fps chemical imaging experiment, in which 0.2 ml of 0.1 M HCl solution was injected into 2.0 ml of 0.1 M NaCl solution at a constant rate of 0.13 ml/s. Spreading of acidic area by injection of HCl was observed in real time. Fig. 8(b) shows an experiment, in which 0.2 ml of 0.1 M HCl was injected into 2.0 ml of neutral phosphate buffer solution (pH 6.86) at a constant

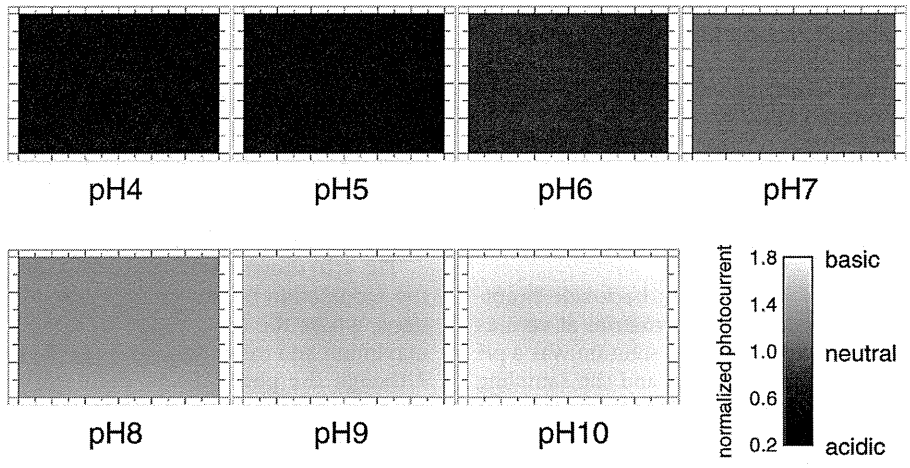

Fig. 6. Chemical images corresponding to different pH values (pH 4–10). These images were generated by interpolating 35 measurement values.

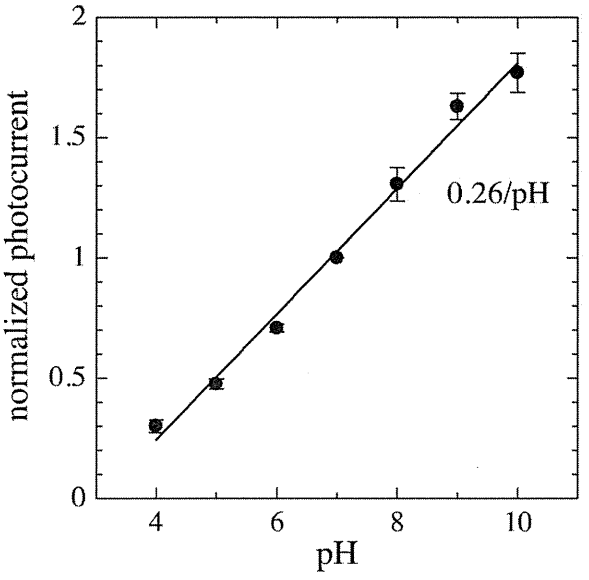

Fig. 7. The normalized photocurrent as a function of the pH value. The black circle is the average of the normalized photocurrent over all 35 pixels and the error bar shows the standard deviation.

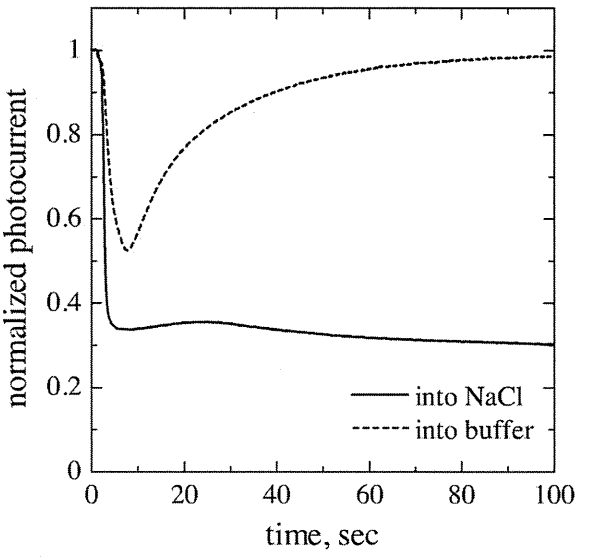

Fig. 9. Time responses of the normalized photocurrent corresponding to the pH value at the center of the LED matrix after injecting HCl solution into NaCl solution or neutral phosphate buffer solution.

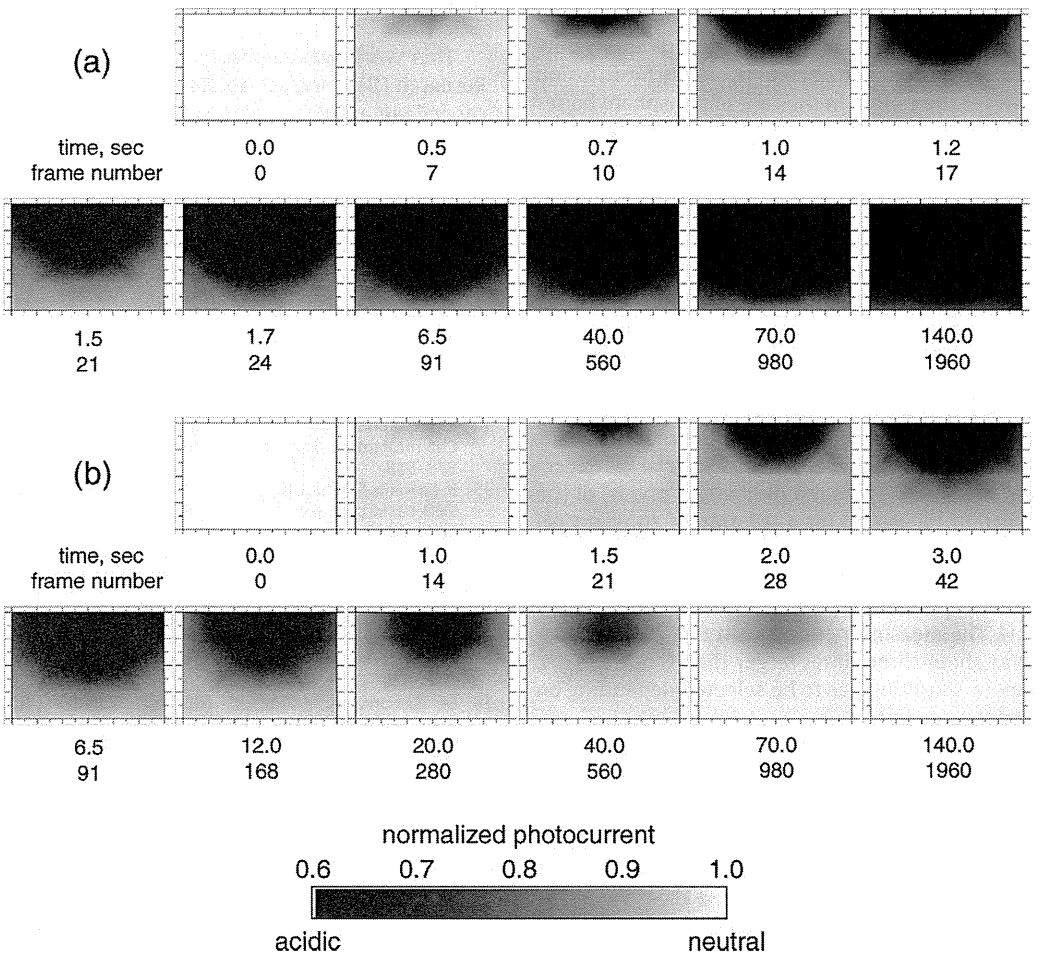

Fig. 8. Snapshots of 14 fps chemical imaging experiment. Spatiotemporal change of pH distribution was recorded after injecting HCl solution into (a) NaCl solution or (b) neutral phosphate buffer solution. These images were generated by interpolating 35 measurement values.

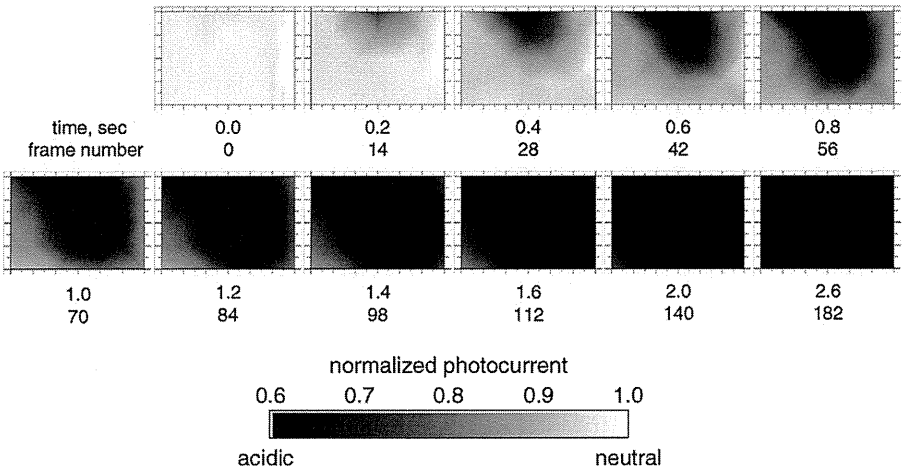

Fig. 10. Snapshots of 70 fps chemical imaging experiment. Spatiotemporal change of pH distribution was recorded after injecting HCl solution into NaCl solution. These images were generated by interpolating 35 measurement values.

rate of 0.13 ml/s. After spreading of acidic area, shrinking of acidic area due to the buffering action,

$$H^+ + HPO_4^{2-} \rightarrow H_2PO_4^-$$

was observed. These experimental results demonstrate the possibility of spatiotemporal recording of chemical reactions by the developed system.

Fig. 9 shows the temporal changes of the normalized photocurrent recorded at the center of the LED matrix. In the case of NaCl solution, the normalized photocurrent decreased rapidly during injection of HCl solution and then decreased slowly by diffusion of hydrogen ions toward the center. In the case of phosphate buffer solution, on the other hand, the normalized photocurrent returned to the initial state due to the buffering action after the decrease by injection of HCl solution.

Chemical imaging at even higher speed is possible by reducing the sampling time per line from 10 ms to 2 ms. In this case it takes 14 ms to scan a frame of 7 lines, which corresponds to a frame rate of about 70 fps. Fig. 10 shows the snapshots of 70 fps chemical imaging experiment with a sampling frequency of 400 kHz. In this experiment, 0.3 ml of 0.1 M HCl solution was injected into 2.0 ml of 0.1 M NaCl solution at a constant rate of 0.13 ml/s. Rapid change of pH distribution was recorded as a smooth movie.

Due to reduction of the measurement time, the measurement error in the 70 fps experiment is larger than that in the 14 fps experiment. The standard deviation (averaged over all 35 pixels) of the normalized photocurrent measured for a solution of constant pH was 0.00182 and 0.00503 in the 14 fps and 70 fps experiments, respectively. Converting these values into pH deviation, the measurement accuracy at 14 fps was about ±0.007 pH and that at 70 fps was about ±0.02 pH. The measurement error in the 70 fps experiment, therefore, was about three times larger than that in 14 fps. Thus, the measurement condition has to be selected depending on the purpose of the measurement.

4. Conclusion

In this study, a high-speed chemical imaging system based on front-side-illuminated LAPS was developed using a two-dimensional array of LEDs. It was demonstrated that front-side illumination was more suitable for high-speed chemical imaging, which would require a wide bandwidth of the modulation frequency. Using the developed system, a rapid change of pH distribution could be visualized by acquiring chemical images at 70 fps.

A chemical imaging system with an even higher temporal resolution is under development, which allows parallel access to all pixels using a two-dimensional array of LEDs modulated independently at different frequencies. Such a high-speed system combined with an optical fiber bundle for arranging measurement pixels at higher density would be useful for analysis of chemical reactions in more detail and applications in the field of biology.

Acknowledgments

This work was supported by JSPS Grant-in-Aid for Scientific Research (B) (contract no. 24310098). A part of this research was carried out at the Machine Shop Division of Fundamental Technology Center, Research Institute of Electrical Communication, Tohoku University.

References

[1] D.G. Hafeman, J.W. Parce, H.M. McConnell, Light-addressable potentiometric sensor for biochemical systems, Science 240 (1988) 1182–1185.
[2] M. Nakao, T. Yoshinobu, H. Iwasaki, Scanning-laser-beam semiconductor pH-imaging sensor, Sensors and Actuators B 20 (1994) 119–123.
[3] Q. Zhang, P. Wang, W.J. Parak, M. George, G. Zhang, A novel design of multi-light LAPS based on digital compensation of frequency domain, Sensors and Actuators B 73 (2001) 152–156.
[4] K. Miyamoto, Y. Kuwabara, S. Kanoh, T. Yoshinobu, T. Wagner, M.J. Schöning, Chemical image scanner based on FDM-LAPS, Sensors and Actuators B 137 (2009) 533–538.
[5] K. Sawada, S. Miura, K. Tomita, T. Nakanishi, H. Tanabe, M. Ishida, T. Ando, Novel CCD-based pH imaging sensor, IEEE Transactions on Electronic Devices 46 (1999) 1846–1849.
[6] T. Hizawa, K. Sawada, H. Takao, M. Ishida, Fabrication of a two-dimensional pH image sensor using a charge transfer technique, Sensors and Actuators B 117 (2006) 509–515.
[7] K. Miyamoto, N. Kosaka, T. Wagner, T. Yoshinobu, High-resolution and high-speed chemical imaging sensor based on optical fiber array, Extended Abstracts of 2012 International Conference on Solid State Devices and Materials (SSDM2012), pp. 368–369.
[8] M. Sartore, M. Adami, C. Nicolini, L. Bousse, S. Mostarshed, D. Hafeman, Minority carrier diffusion length effects on light-addressable potentiometric sensor (LAPS) devices, Sensors and Actuators A 32 (1992) 431–436.

Biographies

Akinori Itabashi was born in Miyagi, Japan, in 1989. He received BE and ME from Department of Electronic Engineering of Tohoku University in 2011 and 2013, respectively. His research subject is on the development of chemical imaging sensor based on the light-addressable potentiometric sensor.

Naoki Kosaka was born in Aomori, Japan, in 1987. He received BE from Department of Electronic Engineering of Tohoku University in 2010, and received ME from

the Graduate School of Biomedical Engineering, Tohoku University in 2012. His research subject is on the development of chemical imaging sensor based on the light-addressable potentiometric sensor.

Ko-ichiro Miyamoto was born in Yamaguchi, Japan, in 1979. He received BE, ME and PhD degrees from Tohoku University in 2002, 2004 and 2006, respectively. His PhD degree is for his study on the bio-molecular sensing using infrared absorption spectroscopy. Since 2006, he is an assistant professor in the Department of Electronic Engineering, Tohoku University. His research subject is on the application of silicon-based chemical sensors for bio-molecular sensing.

Torsten Wagner was born in Mönchengladbach, Germany, in 1978. He received his diploma in 2003 in Electrical Engineering from the University of Applied Sciences Aachen, his master of science in 2003 in model simulation and control from the Coventry University in UK, and his doctoral degree (PhD) in 2008 from the Philips University Marburg in cooperation with the University of Applied Sciences Aachen. His research subjects concern chemical sensors, especially the light-addressable potentiometric sensor and sensor-signal processing. He received a scholarship (2008–2010) from the Japanese Society for the Promotion of Sciences (JSPS) to work at the Tohoku University in Japan, at which he became 2010 an assistant professor.

Michael J. Schöning received his diploma degree in Electrical Engineering (1989) and his PhD in the field of semiconductor-based microsensors for the detection of ions in liquids (1993), both from the Karlsruhe University of Technology. In 1989, he jointed the Institute of Radiochemistry at the Research Centre Karlsruhe. Since 1993, he has been with the Institute of Thin Films and Interfaces (now, Institute of Bio and Nanosystems) at the Research Centre Jülich, and since 1999 he was appointed as full Professor at Aachen University of Applied Sciences, Campus Jülich. Since 2006, he serves as a director of the Peter-Grünberg Institute (PGI-8) at the Aachen University of Applied Sciences. His main research subjects concern silicon-based chemical and biological sensors, thin-film technologies, solid-state physics, microsystem and nano(bio-)technology.

Tatsuo Yoshinobu was born in Kyoto, Japan, in 1964. He received BE, ME, and PhD degrees in electrical engineering from Kyoto University in 1987, 1989, and 1992, respectively, for his study on gas source molecular beam epitaxy of silicon carbide. In 1992, he joined the Institute of Scientific and Industrial Research, Osaka University, where he started the development of silicon-based chemical sensors. From 1999 to 2000, he was a guest scientist at the Research Centre Jülich, Germany. Since 2005, he is a professor for Electronic Engineering at Tohoku University, Sendai, Japan. Since 2008, he is also a professor at the Graduate School of Biomedical Engineering, Tohoku University.

日本機械学会誌　2013. 1　Vol. 116　No.1130

解説

MEMS技術を利用した低侵襲医療・ヘルスケア機器の開発

Development of Minimally Invasive Medical Devices and Healthcare Devices Using MEMS Technology

芳賀　洋一
Yoichi HAGA

◎1992年東北大学医学部卒業．1994～1996年東北厚生年金病院勤務．1996年東北大学大学院工学研究科助手，2003年講師，2004年東北大学先進医工学研究機構（TUBERO）助教授，2008年より現職
◎研究・専門テーマは，マイクロ/ナノテクノロジーを用いた医療・ヘルスケア機器の研究・開発
◎正員，東北大学教授　大学院医工学研究科
（〒980-8579　仙台市青葉区荒巻字青葉6-6）
E-mail：haga@bme.tohoku.ac.jp)

松永　忠雄
Tadao MATSUNAGA

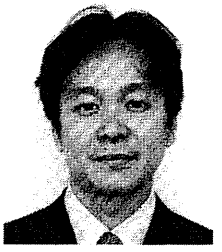

◎1994年佐賀大学理工学部電気工学科卒業，同年曙ブレーキ工業（株）入社，2002年東北大学大学院工学研究科学位取得，博士（工学），2004年東北大学先進医工学研究機構助手（のちに，助教）を経て，2010年より現職
◎研究・専門テーマは，MEMSプロセス，医療・福祉用MEMSデバイス
◎東北大学助教　マイクロシステム融合研究開発センター
（〒980-8579　仙台市青葉区荒巻字青葉6-6）
E-mail：matsunaga@bme.tohoku.ac.jp)

1. はじめに

精密な微細加工技術，とくにマイクロマシニング技術やMEMS（微小電気機械システム）技術などを用いることで，今までにない高機能・多機能な医療ツールが実現できる．その用途は大きく以下の四つに分けることができる．

(1) サンプルを体外に取り出した検査機器（μ-TAS，バイオチップ，DNAチップなど）
(2) 低侵襲医療機器（内視鏡，カテーテルなど）
(3) 体内埋込み機器（神経電極，人工網膜など）
(4) ヘルスケア（健康管理）機器

ここでは，人体に直接作用し，計測や治療を行う「身の回りのマイクロ・ナノ」機器として，(2)，(3)，(4)の機器の開発動向と今後求められる技術，そして展望について述べさせていただく．

2. 低侵襲医療機器

低侵襲医療とは，体を大きく切開せずに内視鏡や，医療用チューブ（カテーテル）などを体内に挿入して従来の手術に匹敵する検査や治療を行うもので，患者の身体的，精神的負担を減らせるほか，入院期間を短縮し医療費の削減にも役立つ．内視鏡には主に胃や腸など消化管に用いられる柔らかく屈曲可能な軟性鏡と，腹腔鏡手術や定位脳手術に用いられる棒状の硬性鏡がある．カテーテルは外径数百μm～数mm程度のポリマ製チューブで，血管内などに挿入して用いられる．内視鏡を用いた治療として体内局所の癌，ポリープの摘出や胆嚢摘出術，カテーテルを用いた血管内治療として血管狭窄部を内側から広げることや脳動脈瘤に詰め物をして破裂を防ぐことなどが行われる．

低侵襲医療の新しい流れとして，腹腔鏡治療などにおいて，従来は皮膚に複数の孔を開けて複数の器具を挿入していたのに対し，共通の一つの孔を用いて複数の器具を挿入するSingle Port Access（SPA）Surgeryや，鼻腔から挿入する経鼻内視鏡，軟性内視鏡を用い胃壁や子宮壁を通り抜けて腹腔内臓器の治療までも行うNOTES（Natural Orifice Transluminal Endoscopic Surgery）などが広く行われてきており，血管内カテーテルでは，高周波アブレーションカテーテルによる心腔内からの不整脈治療などがある．

これらに用いられる内視鏡やカテーテルは，より細く小さく，精度よく，安全かつ確実に検査と治療が行えることが求められている．さまざまな利点の一方で，視野が狭い，操作性が劣る，術者の習熟に時間がかかるなどの欠点もある．さらに低侵襲医療の新しい手法や治療対象の広がりに伴い，術者の習熟が追いつかないなどの問題も出てきている．

このような問題を工学技術により解決する試みがいくつかなされている．たとえば硬性鏡の操作をロボット化したロボット外科手術や，飲み込むことで体内の映像をワイヤレスで体外に送信するカプセル内視鏡がある．ロボット外科手術は体内に挿入するツール内のワイヤを体外の電動モータで牽引し鉗子などを動かすシステムであり，これを軟性内視鏡やカテーテルのような多機能化，細径化とともにシャフトの柔軟性が求められる医療ツールにそのまま適用することは難しい．また，システムが大がかりになる欠点もある．飲み込むと消化管内側の映像をワイヤレスで体外へ送信するカプセル内視鏡は小腸など従来の内視鏡が到達しにくい場所を患者の負担なく観察できる点で有用であるが，体内におけるカプセルの移動や位置合わせの制御は

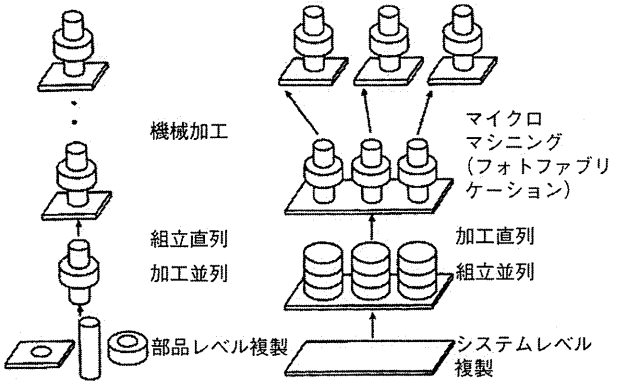

図1　従来の機械加工・組立（左）とフォトファブリケーションによる一括作製（右）

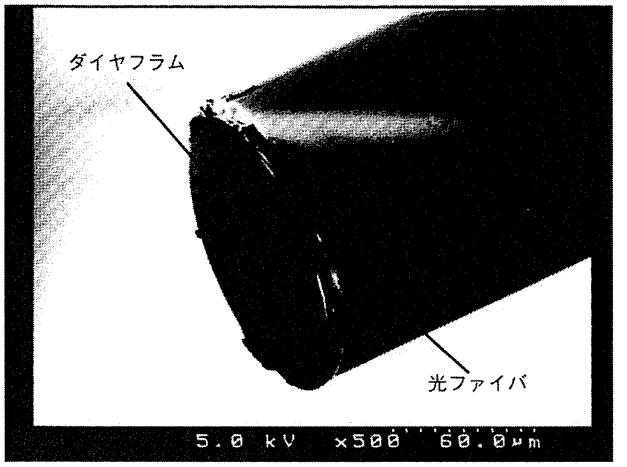

図2　極細径光ファイバ圧力センサ（外径 125 μm）

難しく，現状では一般に行われている生検（バイオプシー）や治療には適さない．また，消化管以外，たとえば血管内でカプセル形状のワイヤレスシステムを用いるには，安全に回収または体内で代謝・分解される必要や，移動の制御，小型化に伴うエネルギー供給の問題などを考慮しなければならない．

このような課題を解決するのに，マイクロマシニング，MEMS などの微細加工技術と新しい材料技術が役立つ．**図1**のようにウェーハレベルで複雑な機械要素を一括に作製可能で量産性に優れた MEMS 技術は，血液や体液を介した感染を防ぐための使い捨て（ディスポーザブル）にも役立つ．今後これらの技術を駆使することにより患者の負担を減らせるばかりでなく，今まで到達が不可能だった部位での検査・治療が可能になるほか，今までにない精密で複雑な検査・治療が可能となる．とくに，マイクロセンサやマイクロアクチュエータを利用することで内視鏡やカテーテルの先で細胞レベル，さらには分子レベルの検査，治療が実現できるようになると期待される．

ピエゾ抵抗効果を利用した半導体ストレンゲージを用いて，体内で用いる医療用のマイクロ力センサや触覚センサ[1]，圧力センサ[2]が試作開発されている．センサは MEMS 技術を用いてシリコン基板上に作製される．一方，光ファイバ先端に外力によってたわむ片持ち梁やダイヤフラムを取り付け，外力によるその変位を光学的に読み取ることで，体内に挿入できる細径の圧力センサや力センサになる．**図2**に直径 125 μm の極細径光ファイバ圧力センサを示す[3]．MEMS 技術により作製された厚さ 0.7 μm の薄いシリコン酸化膜ダイヤフラムが直径 125 μm の光ファイバ端面に形成されており，圧力によるダイヤフラムのたわみを白色光の干渉スペクトル変化で検出する．髪の毛程度に細いので，従来のセンサでは挿入不可能な血管内狭窄部や細血管など狭い部位に挿入でき，精密な局所圧測定を行うことができる．センサ構造体は MEMS プロセスを用いてシリコン基板上に多数のダイヤフラム構造を一括で作製し，その後，反応性イオンエッチング（RIE）で貫通エッチングを行い，ダイヤフラムを持った多数の円柱形状パーツを一括作製する．これをガラスキャピラリ内で光ファイバ端面に金属層を介して円柱パーツを接合した後，シリコン円柱部を選択的にエッチング除去する．センサ部が小さいので 1 回のプロセスで 1 枚のシリコンウェーハから数十万個という膨大な数のダイヤフラム構造体を得ることができる．

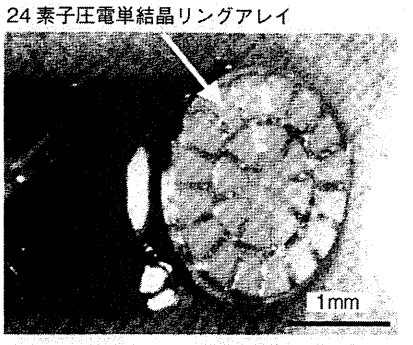

図3　血管内前方視超音波内視鏡（外径 2.5mm）

超音波検査法は，体内組織からの超音波反射エコーを利用して体内の構造を可視化する方法で，超音波プローブを小さくすることで体内に持ち込むことが可能になり，体外から観察するよりも精密な画像を得ることができる．内視鏡先端に超音波プローブを搭載したものやカテーテルに搭載され血管内で用いる超音波内視鏡が広く臨床に用いられている．カテーテル進行方向の血管壁と病的な狭窄部を超音波イメージングにより三次元的な可視化を行い，血管内治療を安全かつ確実に行うことを目指し，**図3**に示すような直径 3mm のカテーテル先端搭載用前方視超音波プローブを開発している[4]．微小な振動子でも高い超音波強度，高感度を実現するため PZT よりも圧電特性に優れる圧電単結晶の PMN-PT を超音波振動子として用い微細加工したもので，これをカテーテル端面上に円周状に 24 個並べ，それぞれが超音波の送信と受信を行う．そのほか，超音波トランスデューサとして，機能性材料を使わずに静電駆動により超音波トランスデューサとなる量産性に適した CMUTs なども医療用応用向けに開発され，血管内超音波内視鏡としての試作も試みられている[5]．また，内視鏡やカテーテル先端から集束した超音波を組織に照射し，病変組織に働きかけ治療する試みもなされている[6]．

一般に，胃カメラなど消化管検査などに用いられる軟性内視鏡の屈曲や，組織をつかむ鉗子の動作は，シャフトを通したワイヤを体外から牽引することで行っており，これは内視鏡手術ツールをロボット化したロボット外科手術でも同様である．ワイヤ牽引を用いた駆動は，ツールを細く小さくする程シャフトが変形しやすくなるため先端の精密

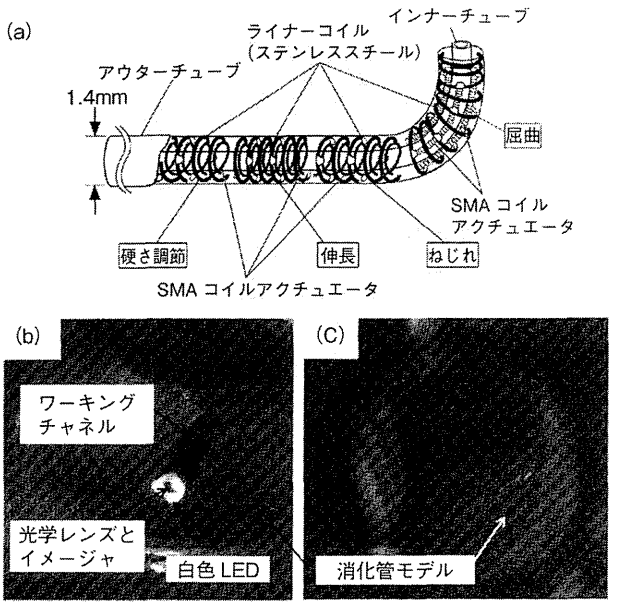

図 4　能動屈曲電子内視鏡　(外径 3.9mm)

(a) 形状記憶合金を用いた能動カテーテルの構成図
(b) 多方向能動屈曲電子内視鏡を腸モデル内に挿入した様子
(c) 先端のイメージャから腸モデルを撮像した様子

な動作ができなくなる．とくに曲がりくねった先では自在な操作はできない．低侵襲医療ツールにマイクロアクチュエータを組み込むことができれば，細く柔らかい機器の先で精密な動作が可能になる．ワイヤに代わる医療用マイクロアクチュエータとして，比較的大きな変位と力が出せる形状記憶合金（SMA），ポリマアクチュエータなどが提案されている．たとえばSMAをカテーテルや内視鏡など医療ツールの先端部に搭載することで，**図 4** のように屈曲，ねじれ回転や伸縮などさまざまな動きを実現できる[7]．具体的な用途としてたとえば，腸の通過障害である腸閉塞の際に腸内容を吸引して減圧治療を行うポリマチューブ先端に屈曲機構を搭載し，病変部に容易に到達できるようにした屈曲チューブなどがある[8]．SMAを用いて多方向に曲がることができる能動屈曲機構先端にCCDやCMOSイメージャを搭載した能動屈曲電子内視鏡は，体内の奥深くに容易に到達し，必要に応じチューブ内腔を通して生検や治療が行えるほか，屈曲機構を低コスト化できるので使い捨て化も可能と期待される[9]．有線は一時的な挿入であればエネルギー供給や回収が容易で，チューブの途中にスイッチング回路を分布させることで配線数の増加を低減した多関節化や多機能化もできる[10]．

体内に挿入または留置する医療機器の多くは穿刺針や内視鏡の鉗子口を通して体内に挿入されることから一般に円筒形状をしており，半導体微細加工技術など平面基板をベースに発展してきたMEMS技術がそのまま適応できない場合が多い．とくにカテーテルなど低侵襲医療ツールの多くは貫通穴を持ち，血管造影剤や薬剤の注入，ガイドワイヤなどさらに細い医療ツール挿入のために必要なことから，パーツをカテーテル内腔に配置して貫通穴の機能をなくすことは望ましくない．円筒形状の体内埋込みデバイス，カプセル内視鏡においても，従来のMEMS技術をそのまま適応すると内腔を有効に利用できない．

図 5 のように電気配線やパッドを形成したフレキシブル基板をらせん形状に巻くことで内腔の確保と柔軟性を実現できるが，基板の厚さや曲率の制限，巻き付けた際の基板端同士のアライメント誤差に気をつける必要がある．図では熱可塑性樹脂である液晶ポリマーを基板材料として用い形状保持を容易にし，はんだバンプを形成した集積回路（ダミー）の実装も行った．回路を巻き付け可能に柔軟にする方法として，プラスチックフィルム上に有機トランジスタを形成し，感圧導電性ゴムと組み合わせカテーテルへらせん形状に巻き付け分布型圧力センサとした例もある[11]．円筒形状の医療ツールに直接微細加工を行う試みがいくつか行われており，たとえばカテーテルの外壁に銅めっきを施しレーザアブレーションを用いて複数の螺旋配線を形成した例がある[12]．筆者らは多方向に屈曲するSMAアクチュエータ作製のために形状記憶済みTi-Ni合金製SMAチューブのフェムト秒レーザ加工を試み[13]，またチューブに転動露光を利用したフォトリソグラフィーと電解エッチングを行い，三つのジグザグばね構造を有したSMAマイクロアクチュエータを試作した[14]．さらに非平面へMEMSプロセスを適用し，直径2mm～3mmのガラスチューブ上にレーザ照射を利用したマスクレスフォトリソグラフィーを行い金属ソレノイドコイルパターンや絶縁層を介した多層金属パターンを試作した[15]．これを用いて直径2mmのMRI（磁気共鳴イメージング）受信コイルをカテーテル先端付近に搭載した体腔内MRIプローブを開発した例を**図 6** に示す[16]．従来のMRIでは体外の励起コイルにより組織から発生する核磁気共鳴（NMR）信号を体外の受信コイルによって受信し像が形成される．たとえば血管内に小型受信コイルを挿入し，撮像対象の近くで受信することで信号強度とS/N比が向上し**図 6 (b)** のように高解像度のイメージングができる．これにより動脈硬化や粥状硬化，動脈瘤などの病変をより精密に観察，診断できると期待される．コイルはポリイミドチューブ表面の円筒面上へフォトレジストのパターニングと，レジストを型にした銅の電解めっきを用いて作製される．さらに絶縁層を形成し同様の配線形成プロセスを繰り返すことでコイルを多層化でき性能を向上できる（**図 6 (c)**）．NMR信号の受信と体外への伝送を効率よく行うためにコイル近くに回路を搭載するが，コイル周辺の組織によって最適な共振周波数，インピーダンスが僅かに変動することから，外部からの電圧コントロールにより容量を可変できる集積回路をカテーテルに搭載できるよう小型に設計，試作している．

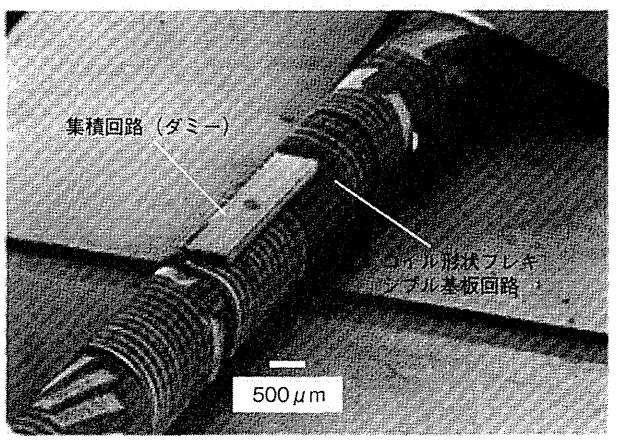

図 5　コイル形状のフレキシブル基板と電子パーツの搭載

3. 体内埋込み機器

体内に留置して神経刺激を行う体内埋込みデバイスとして心臓ペースメーカや人工内耳がすでに広く普及しているが，脳神経との電気的インタフェースを行うための体内埋込みデバイスとして神経束からの信号導出システムおよび神経刺激電極がMEMS技術を用いて開発されている[17]．また，網膜色素変性症など網膜病変により失明した患者に対して網膜刺激型人工視覚デバイスが[18]，事故による神経の切断などで動かなくなった筋肉に対してワイヤレスで筋肉に電気信号を与えて動かす体内埋込み型電気刺激装置[19]が，それぞれ開発されている．

体内埋込み型のDDS（薬物送達システム）デバイスは，一般に埋込み後の薬剤放出の精密なコントロールや薬の種類の切り換えは難しい．MEMS技術を利用して体外からワイヤレスで電気的に薬剤放出をコントロールできる埋込み型DDSデバイスが開発されている．シリコン基板をエッチングして作られた複数の微小ウェルの中に薬剤が封入されており，ウェルをふさぐ蓋を，通電による抵抗加熱または電気分解によって個別に破壊することにより薬剤放出のタイミングと量をコントロールする[20]．

埋込みデバイスとして胸腹部動脈瘤手術中に体内に留置し，術後の血管内局所血圧モニタする小型圧力センサをアメリカCardiomems社などが開発しており，高周波を用いて体外からワイヤレスで給電と信号読み出しを行う．埋込まれるセンサのサイズはたとえば30mm × 5mmで厚さ1.5mm程度となっている[21]．

4. ヘルスケア（健康管理）機器

健康への社会的関心の高まりに伴い，ヘルスケア（健康管理）分野へのMEMS応用の期待が増している．MEMS技術を用いることで新たな計測が可能になるばかりでなく，デバイスを小さく軽くでき，体表や衣服に常に身に着けるウェアラブル機器としての時間や場所にしばられない生体情報モニタリングが期待される．MEMSを用いたウェアラブルセンサの実例として，アメリカンフットボールプレイヤーのヘルメット内に加速度センサを複数個搭載し，頭部への衝撃をセンシングすることで失神の検知やけがの予防に役立てることが行われており[22]，けがをしたスポーツ選手がリハビリテーションを行う際に呼吸，心拍数，体温や血圧などをモニタし運動量と訓練内容を最適化する試みもなされている[23]．

前述の前方視血管内超音波内視鏡の作製技術を応用し，超音波トランスデューサ素子が二次元アレイ状に並んだシート形状のウェアラブル血圧センサを開発した[24]．一般に血圧を測る際は腕や手首などにマンシェットを巻き付けて圧迫するカフ圧迫法が用いられるが，使用者に計測を意識させることなく間欠的に血圧をモニタリングすることは難しい．皮膚上に置いた超音波トランスデューサからパルス波を出し皮下の血管の前壁と後壁の反射エコーを利用し，その遅れ時間を計測することで，血管壁を一定の硬さを持つ管と想定し血管径の変化を計算し，間接的に血圧を測定できる．素子を二次元アレイ状に配置し，ちょうど血管の上に位置し血管径の変化がみられる素子からの信号のみを利用することで皮膚上の超音波トランスデューサ素子と皮下の血管の位置合わせの問題を解決している．**図7**に

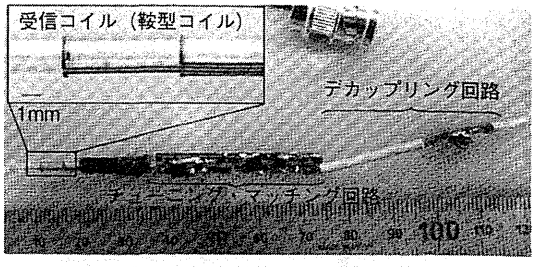

(a) MRIプローブ（外径2mmの1層サドルコイル）

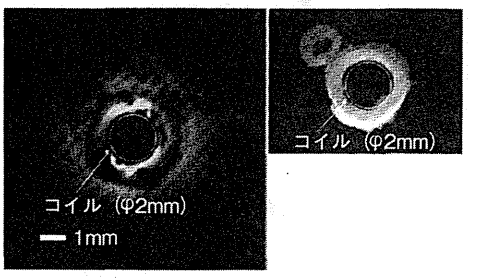

(b) 摘出血管（右）と撮像結果（左）（ブタ鎖骨下動脈）

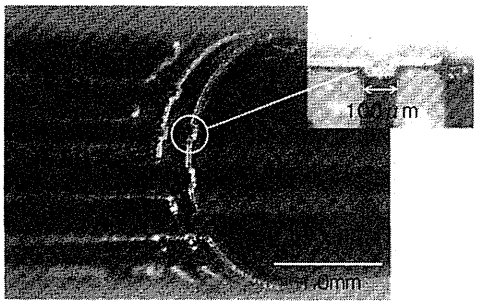

(c) 多層コイル

図6　体腔内MRIプローブ

装置構成と結果を示すが，手首近くの橈骨動脈において血管内圧の変化と同様の波形が得られている．実使用の際は装着時に従来の血圧測定法を用いて校正を行う．微細加工技術を用いることで薄く軽い超音波トランスデューサアレイシートが実現できる．皮膚上に貼付するデバイスとして，伸縮性基板材料に電子デバイスを形成することも試みられており，今後の応用展開が期待される[25]．

乳酸や血糖，ストレス物質など生体成分を採血せずモニタリングすることを目指して，皮膚に微小な針を刺し，微小透析（マイクロダイアリシス）を行い，皮下組織液に含まれる生体成分を経皮的に取り出し計測することを行っている．**図8**は直径約200 μmの細径金属針の外壁にポリマー（ポリイミド）層による微小流路を形成したもので，流路上のフタのうち皮下に位置する部分に貫通穴を設け，流路に液を循環させる．作製は電着，レーザアブレーション，電解めっきによる犠牲層作製などを用いて行う．マウスの皮下に刺入，留置し，血中の乳酸値と皮下回収液中乳酸の相関が確認できた．乳酸の計測は運動強度の定量化などに役立つ[26]．円皮針と呼ばれる針の付いた絆創膏を皮膚に貼付し継続的な経穴刺激を行う構成にならって，将来，絆創膏上にマイクロポンプと微小透析用タンク，ワイヤレス通信機能を組み合わせ，採血に頼らないウェアラブルな生体成分モニタ装置を目指している．

これらウェアラブルヘルスケア機器は今後，携帯電話やスマートフォンなどを経由してネットワーク上でデータの

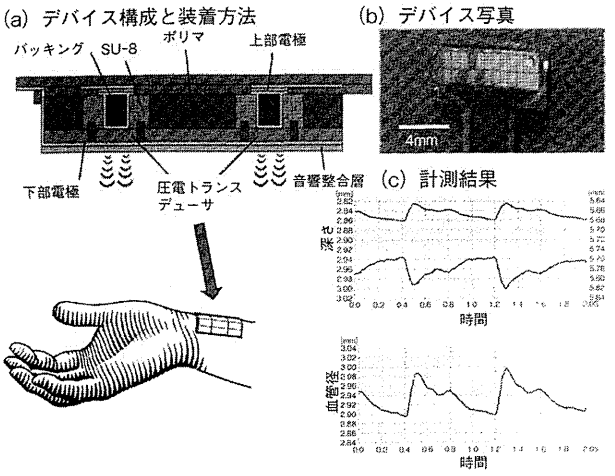

図7　超音波血管径計測によるウェアラブル血圧センサシート

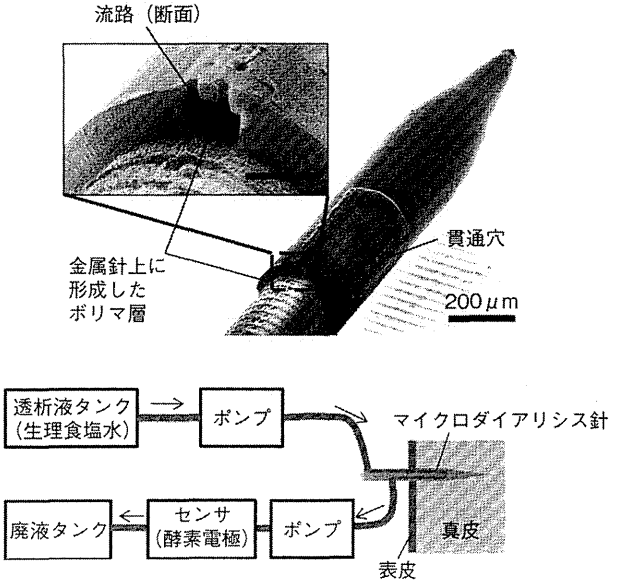

図8　生体成分計測用微小流路を形成した金属針

蓄積や分析を行い，ユーザや医療従事者への有用なフィードバックを行うようになると期待されている[27]．

5. おわりに

低侵襲医療機器，体内埋込み機器など人体に対して用いられる医療機器開発には独特の状況や要求が伴う．具体的には，感染を防ぐための消毒およびディスポーザブル（使い捨て）化の要求，市販前の安全性確認と医療機器としての許認可，臨床医師がユーザーとして手技を行うこと，さらに特殊な販路などがある．また，開発側からみると，少量多品種，ディスポーザブル化による消費量の多さ，効果が高ければデバイスの単価が比較的高く設定できる場合がある，といったマイクロマシン/MEMS技術と合致した利点がある一方，医療機器としての安全性の確保や許認可に費用と時間がかかるリスクが大きな足かせとなっている．MEMS作製に用いられる高額でランニングコストのかかる製造設備を導入し長期にわたる開発とその後の製造を行うことは一般の医療機器メーカには難しく，実用化のためには製造プロセスの一部を請け負うファウンダリーの活用や，その他さまざまな工夫や新たな仕組み作りが構造や作製上の工夫に併せて求められる．一方で，微細加工技術が提供できる高い信頼性，高機能性は今後の医療に不可欠であり，さまざまな障害はあるものの，微細加工技術分野における今後の技術的進歩と，患者および医療従事者の要望に支えられ，今後いっそう，新たな医療機器の開発が行われていくと期待される．

（原稿受付　2012年11月7日）

●文　献
(1) Takizawa, H. ほか, Development of a Microfine Active Bending Catheter Equipped with MIF Tactile Sensors, *Tech. Digest MEMS'99* (1999), 412.
(2) Kalvesten, E. ほか, The first surface micromachined pressure sensor for cardiovascular pressure measurements, *Tech. Digest MEMS'98*, (1998), 574.
(3) Katsumata, T. ほか, Micromachined 125 μm Diameter Ultra Miniature Fiber-Optic Pressure Sensor for Catheter, *Trans. IEE of Japan*, **120**-E-2 (2000), 58.
(4) 陳俊傑 ほか, 血管内低侵襲治療のための前方視超音波イメージャーの開発, 生体医工学, **43**-4 (2005), 553.
(5) Yeh, D. T. ほか, 3-D Ultrasound Imaging Using a Forward-Looking CMUT Ring Array for Intravascular/Intracardiac Applications, *IEEE Trans. Ultrason. Ferroelectr. Freq. Control*, **53** (2006), 1202.
(6) 安居晃啓 ほか, 小型収束超音波トランスデューサを用いた内視鏡的治療デバイス, 電気学会論文誌 E, **127**-2 (2007), 69.
(7) 芳賀洋一 ほか, 屈曲，ねじれ，伸長能動カテーテルの電気めっきによる組み立て, 電気学会論文誌 E, **120**-11 (2000), 515.
(8) 水島昌徳 ほか, 形状記憶合金を用いた腸閉塞治療用能動カテーテル, 日本コンピュータ外科学会誌, **5** (2004), 23.
(9) 牧志 渉 ほか, 使い捨て化と細径化を目指した形状記憶合金を用いた能動屈曲電子内視鏡の開発，電気学会論文誌 E, **131**-3 (2011), 102.
(10) Park, K. ほか, A Multilink Active Catheter with Polyimide-Based Integrated CMOS Interface Circuits, *J. Microelectromech. Syst.*, **8**-4 (1999), 349.
(11) Sekitani, T. ほか, Flexible Organic Transistors and Circuits with Extreme Bending Stability, Nature Materials, **9** (2010), 1015.
(12) 三澤 裕 ほか, マイクロカテーテル微細加工技術, 国際マイクロマシンシンポジウム, (1995-11), 123.
(13) Haga, Y. ほか, Medical and Welfare Applications of Shape Memory Alloy Microcoil Actuators, *Smart Mater. Struct.*, **14**-5 (2005), 266.
(14) 幸田 貴 ほか, 非平面フォトファブリケーションによる形状記憶合金パイプからのアクチュエータ作製，電気学会論文誌 E, **123**-5 (2003), 158.
(15) Goto, S. ほか, Photolithography on Cylindrical Substrates for Realization of High-Functional Tube-Shaped Micro-Tools, *Proc. Sens. Symp. Sens. Micromachines Appl. Syst.*, (2005-10), 112.
(16) 五島彰二 ほか, カテーテル実装に適した血管内 MRI プローブの開発, 電気学会論文誌 E, **128**-10 (2008), 389.
(17) Wise, K. D. ほか, Wireless Implantable Microsystems : High-Density Electronic Interfaces to the Nervous System, *Proc. IEEE*, **92**-1 (2004), 76.
(18) Schwarz, M ほか, Single chip CMOS imagers and flexible microelectronic stimulators for a retina implant system, *Sens. Act.*, A **83** (2000), 40.
(19) Loeb, G. E. ほか, Design and Fabrication of Hermetic Microelectronic Implants, *Proc. IEEE-EMBS Special Topic Conf. on Microtech. in Med. and Biol*, (2000-10), 455.
(20) LaVan, D. A. ほか, Small-scale systems for in vivo drug delivery, *Nature Biotechnology*, **21** (2003), 1184.
(21) Allen, M. G., Micromachined Endovascularly-implantable Wireless Aneurysm Pressure Sensors : from Concept to Clinic, *Proc. Int. Conf. Solid-State Sensors and Actuators (Transducers '05)*, (2005-6), 275.
(22) Jones, W. D. ほか, Helmets Sense The Hard Knocks, *IEEE Spectrum*, (2007-10), 8.
(23) Glaros, C. ほか, A Wearable Intelligent System for Monitoring Health Condition and Rehabilitation of Running Athletes, *Proc. IEEE Conf. on Information Technology Applications in Biomedicine*, (2003), 276.
(24) 鈴木大地 ほか, 超音波計測を用いたウェアラブル血圧センサの開発, 第51回日本生体医工学会大会, (2012-5).
(25) Kim, D. H. ほか, Epidermal Electronics, *Science*, **333** (2011), 838.
(26) Tsuruoka, N. ほか, Development of Minimally Invasive Microdialysis Needle for Continuous Monitoring of Biological Substances, *Tech. Digest MEMS 2012*, (2012-1), 941.
(27) 小谷卓也 ほか, つながる健康機器に電機が集まる, 日経エレクトロニクス, **955** (2007-7), 47.

Measurement of blood glucose by infrared spectroscopy using hollow-optical fiber probe

Y. Tanaka, S. Kino, and Y. Matsuura
Graduate School of Biomedical Engineering, Tohoku University
6-6-05 Aoba-Sendai 980-8579, Japan

ABSTRACT

An infrared spectroscopy system based on a hollow-optical fiber probe for measurement of blood glucose concentration is developed. The probe consists of a flexible hollow-optical fiber and an ATR prism attached at the distal end of the fiber. This flexible probe enables measurement of oral mucosa and ear lobes that have blood capillaries near the skin surface. Experimental results show that absorption peaks of blood glucose are detected by the system.

Keywords: Hollow-optical fiber, FT-IR, ATR, Glucose measurement

1. INTRODUCTION

Diabetes is one of the most serious social problems in the world and patients have to check their blood glucose level on a frequent basis by collecting blood. This procedure causes not only a load to patients but also a risk of infectious diseases. Although some systems based on near infrared spectroscopy (NIR) are suggested as a non-invasive method of blood glucose measurement [1, 2], those systems still have problems in the accuracy and reliability. One of the reasons for these problems is that NIR analyses detect harmonic overtones of target molecular vibrations. Usually many other overtone peaks are imposed on the target vibrations and therefore, complicated multivariate statistics such as principal component analysis (PCR) are necessary for quantitative analysis.

In this report, we examined non-invasive blood glucose monitoring system based on Fourier transform infrared spectroscopy (FT-IR). Mid infrared spectroscopy (MIR) detects the fundamental vibrations of molecules. Therefore, absorption intensities are higher than those of NIR and complicated calculations that tend to cause inaccuracy are not necessary. Heise *et al.* reported that they determined glucose levels of whole blood from the mid-infrared absorption spectra [3]. Some groups reported that they attempted to measure blood glucose levels *in vivo* by taking MIR spectra of finger using an attenuated total reflection (ATR) prism[4]. Since ATR spectroscopy provides higher signal levels than that of reflection measurement, it enables high signal-to-noise measurement. When applying a common ATR system *in vivo*, however, body sites for measurement are limited because the sites should be touched by the ATR prism involved in the system. To solve this problem, in this report, we developed an ATR system utilizing a flexible hollow-optical fiber probe. The probe is based on an infrared hollow-optical fiber with an ATR prism attached on the distal end. We show experimental results for *in-vivo* quantitative detection of blood glucose.

2. *IN-VITRO* MEASUREMENT OF BLOOD GLUCOSE CONCENTRATION

Figure 1 shows an experimental setup for measurement of ATR spectroscopy. Infrared light emitted from the FTIR spectrometer is focused onto the input end of hollow optical fiber by using an off-axis mirror. We used a hollow optical fiber based on a flexible polycarbonate tube having inner coating of silver reflection layer with a cyclic-olefin polymer overcoat. This type of hollow optical fiber transmits a wide range from 2 to 20 μm of the infrared with low losses [5]. The inner diameter of fiber is 2 mm and the length is 1 m. As shown in the inset of Fig. 1, a diamond ATR prism is attached at the output end of the fiber. In the prism, incident light is reflected twice and then, the evanescent field detects absorption of the sample that touches on the prism surface. The reflected light is deflected by the beam splitter and detected by a HgCdTe detector.

Optical Fibers and Sensors for Medical Diagnostics and Treatment Applications XIII,
edited by Israel Gannot, Proc. of SPIE Vol. 8576, 85760T · © 2013 SPIE
CCC code: 1605-7422/13/$18 · doi: 10.1117/12.2008279

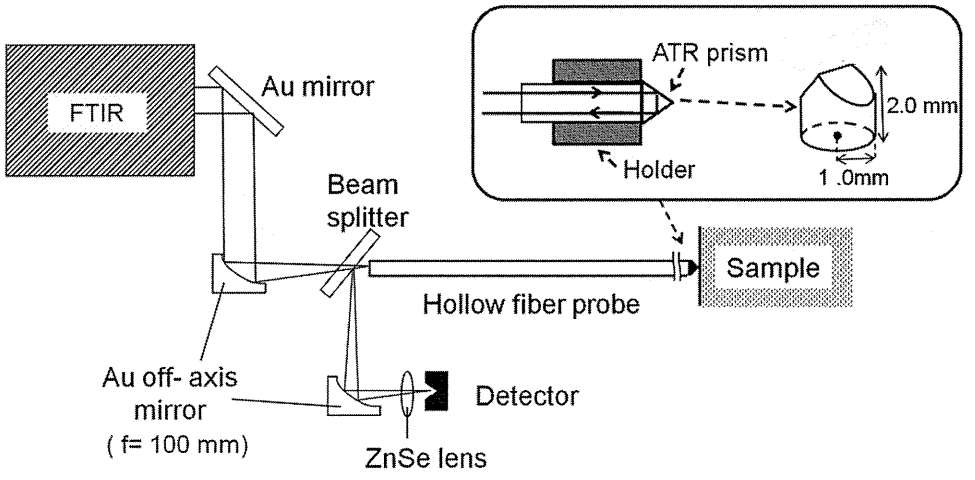

Figure 1. Experimental setup for measurement of ATR spectroscopy.

Figure 2 shows absorbance spectra of glucose solutions in water with various concentrations. In this measurement, the ATR prism was dipped in the solution and the frequency resolutions of 4 cm^{-1} and 128 times of integration are applied. Strong peaks originated from the OH-stretching band and the OH-bending band of water molecules appear near 3300 $cm^{-1}$and 1700 cm^{-1}, respectively. An IR vibrational band assigned to glucose, which is derived from COH stretching band, is shown around 1040 cm^{-1}. The peak around 2300cm^{-1} is caused by CO_2 gas band inside the fiber. When glucose concentration decreases, peak intensities of OH-bands increase while the peak of glucose decreases. The reason of this phenomenon is that a number of water molecule on the light axis increases by decreasing a number of glucose molecule. The correlation between the peak intensities of an OH-band and glucose are useful when suppressing effects of change in background intensity that is due to, for example, variation of the pressure on the sample surface. By taking the ratio of these peaks, only contribution of change in glucose level can be detected. In Fig. 3, ratios between two peaks are plotted as a function of glucose concentration. It is shown that these calculated ratios are proportional to the glucose concentration.

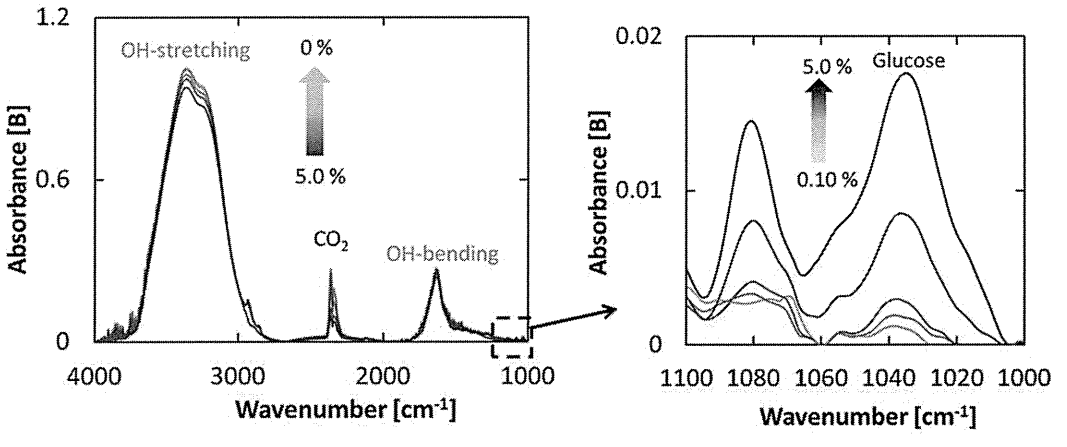

Figure 2. Absorbance spectra of glucose solutions with various concentrations

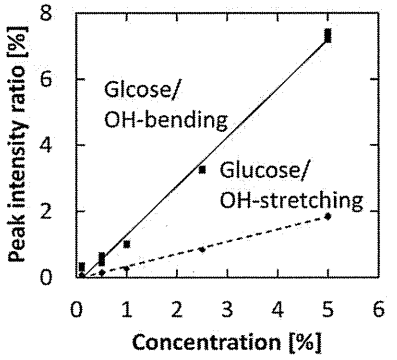

Figure 3. Peak intensity ratio of glucose to each OH band

We also performed similar measurements by using pig's whole blood that contains glucose of various concentrations. In the experiment, the hematocrit value is set to about 40 % that is equivalent to that in human whole blood. As shown in Fig. 4, the peak of glucose is distinguished from those of other blood components. Peak intensity ratio of glucose to each OH band in pig's whole blood is shown in Fig. 5. We confirmed the linear relationship between the ratios and glucose concentrations.

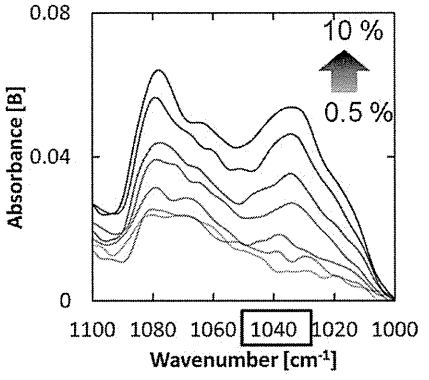

Figure 4. Absorbance spectra of pig's whole blood dissolved glucose with various concentrations

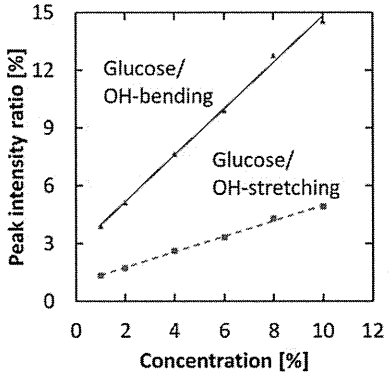

Figure 5. Peak intensity ratios of glucose to each OH band in pig's whole blood

3. *IN-VIVO* MEASUREMENT OF BLOOD GLUCOSE CONCENTRATION

We firstly applied this probe to oral mucosa that is soft and moist and thus, small variation in measurements due to change in applying pressure is expected. Figure 6 shows absorbance spectra of oral mucosa measured *in vivo*. In this experiment, a mouth was washed with water to improve contact of prism surface to mucosa. When measurements were repeatedly performed, the prism was washed with acetone and dried in N_2 gas to clean the prism surface. As shown in Fig. 6, an absorption peak originated from glucose is indicated around 1040 cm^{-1} as with the spectra taken *in vitro*.

After a healthy volunteer took 75 g sugar, we measured his blood sugar level and ATR spectra of oral mucosa at half-hour intervals. Reference blood-glucose levels were measured by using a glucose meter which is based on blood collection by finger puncture. Relationship between reference blood-sugar levels and peak intensities of glucose is shown in Fig. 7. Correlation of these two values was high, however, we found that measurement errors in every measurement are not small, which may cause a problem in reproducibility.

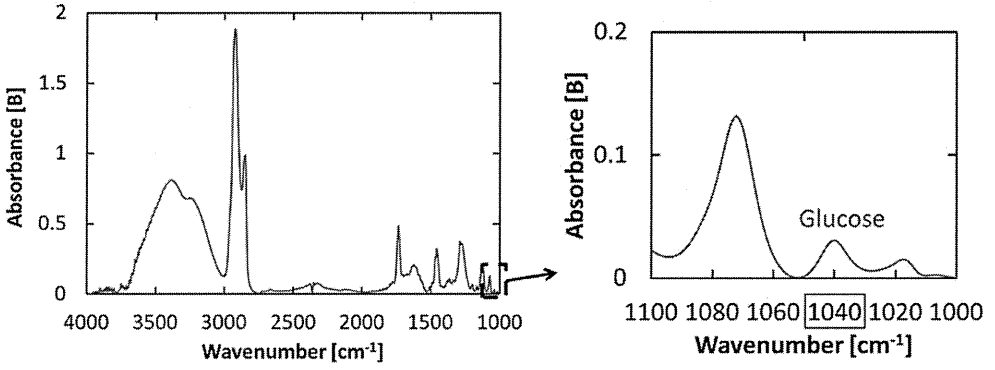

Figure 6. Absorbance spectra of healthy oral mucosa

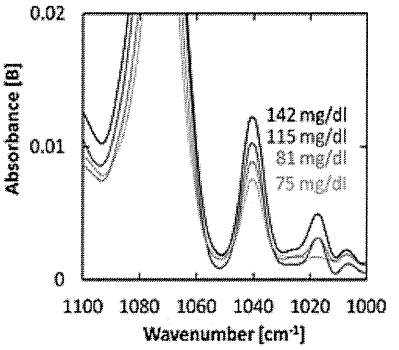

Figure 7. Relationship between blood sugar level and peak intensity of glucose

Next we applied the probe to ear lobes that are easily accessed by the probe. Ear robes are similar to oral mucosa in that blood capillaries are near the skin surface. In the measurement of oral mucosa, we experienced measurement errors that are mainly attributed to changes in the pressure applied to the sample surface. This problem may be solved by applying a reference material which uniformly penetrates into the skin so as to suppress the error due to applying pressure. We tried to use hydrocarbon oil called Squalane as a reference material. Figure 8 shows comparison of absorption spectra of pure water and Squalane. Squalane has the characteristic peaks at 2922, 1462, and 1377 $cm^{-1}$and we confirmed that there is no peak overlapping the 1040 cm^{-1} glucose absorption peak.

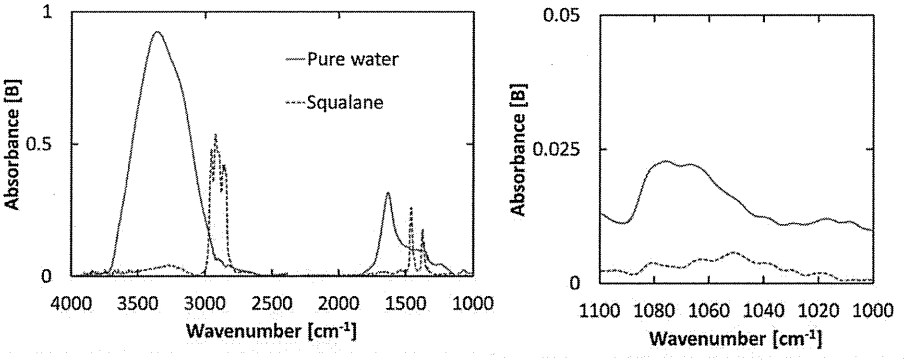

Figure 8. Comparison of absorption spectra between pure water and Squalane

Figure 9 shows absorbance spectra of ear lobes measured after applying Squalane. Five spectra were measured consecutively and the prism surface was cleaned each time. The peak of glucose at 1040cm^{-1}and those of Squalane at 2922cm^{-1}, 1462 cm^{-1} and 1377cm^{-1}are clearly seen. We calculated the ratio of glucose's peak height to those of Squalane and the OH-stretch and then evaluate variation coefficient of measured values. As shown in the result in Table 1, measurement errors are largely reduced by using Squalane as a reference material.

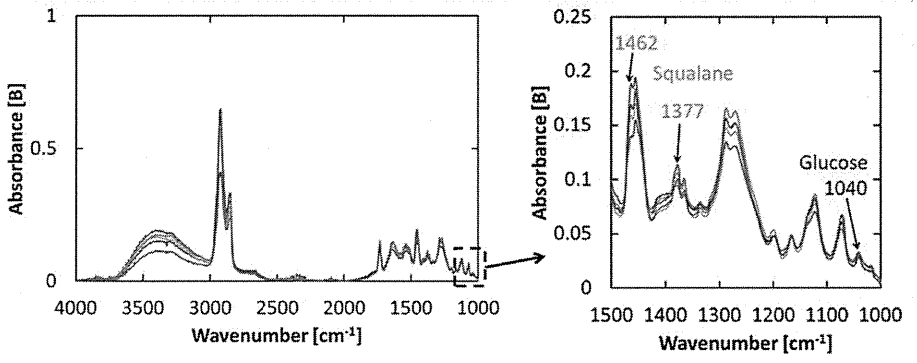

Figure 9. Absorbance spectra of ear lobe with Squalane

Table 1. Variation coefficient of peak intensity ratio of glucose to Squalane and OH-stretch

	Squalane		OH-stretching
Peak intensity ratio	1040 cm^{-1} /1462 cm^{-1}	1040 cm^{-1} /1377 cm^{-1}	1040 cm^{-1}/3400 cm^{-1}
variation coefficient [%] =SD/Ave.	11.16	8.84	22.52

4. CONCLUSION

We developed a non-invasive glucose monitoring system based on mid-IR ATR spectroscopy using a flexible hollow-optical fiber probe. In measurement of oral mucosa and ear lobe, we successfully measured blood glucose levels by detecting a peak intensity of glucose absorption bands. It is known that ATR spectroscopy has limitation in penetration depth that is around a few micrometer and thus, it is difficult to approach to blood capillary network. In our case, it is inferred that tissue water in the stratum content that are strongly correlated to blood components is detected. The experimental results showed that this method is useful for monitoring blood glucose. However, the measurement reproducibility is not high enough even when applied a reference material such as Squalane before measurement. We are working on the investigation of a multi reflection ATR prism which has flat contact area to achieve high sensitivity and high reproducibility.

REFERENCES

[1] K. Maruo, M. Tsurugi, J. Chin, T. Ota, H. Arimoto, Y. Yamada, M. Tamura, M. Ishii, Y. Ozaki, "Noninvasive Blood Glucose Assay Using a Newly Developed Near-Infrared System", IEEE journal of selected topics in quantum electronics 9(2), 322-330 (2003)

[2] Y. Miyauchi, T. Horiguchi, H.Ishizawa, S. Tezuka, H. Hara, "Basis Examination for Development of Noninvasive Blood Glucose Measuring Instrument by Near-Infrared Confocal Optical System", Proc. SICE annual conference , 3427-3429(2010)

[3] H.M. Heise, R. Marbach, "Multivariate determination of glucose in whole blood by attenuated total reflection infrared spectroscopy", Anal. Chem 61(18), 2009-2015 (1989)

[4] H. Ishizawa, A. Muro, T. Takano, K. Honda, H. Kanai, "Non-invasive Blood Glucose Measurement Based on ATR Infrared Spectroscopy", Proc. SICE annual conference , 321-324(2008)

[5] Y. Matsuura, "Basics of Optical Fibers for Medical Applications ", The Journal of Japan Society for Laser Medicine 31(4), 407- 411(2011)

DNA Research **20**, 255–262, (2013)
Advance Access publication on 29 March 2013
doi:10.1093/dnares/dst007

Development and Characterization of cDNA Resources for the Common Marmoset: One of the Experimental Primate Models

Shoji Tatsumoto[1,†], Naoki Adati[1,‡], Yasushi Tohtoki[1,¶], Yoshiyuki Sakaki[1,§], Thorsten Boroviak[2], Sonoko Habu[3], Hideyuki Okano[4], Hiroshi Suemizu[5], Erika Sasaki[6], and Masanobu Satake[7,*]

RIKEN Genomic Sciences Center, Suehiro-cho 1-7-22, Tsurumi-ku, Yokohama 230-0045, Japan[1]; Centre for Stem Cell Research, Wellcome Trust and Medical Research Council Stem Cell Institute, University of Cambridge, Tennis Court Road, Cambridge CB2 1QR, UK[2]; Department of Immunology, Juntendo University School of Medicine, Hongo 2-1-1, Bunkyo-ku, Tokyo 113-8421, Japan[3]; Department of Physiology, School of Medicine, Keio University, Shinano-machi 35, Shinjyuku-ku, Tokyo 160-8582, Japan[4]; Biomedical Research Department, Central Institute for Experimental Animals, Tonomachi 3-25-12, Kawasaki-ku, Kawasaki 210-0821, Japan[5]; Department of Applied Developmental Biology, Central Institute for Experimental Animals, Tonomachi 3-25-12, Kawasaki-ku, Kawasaki 210-0821, Japan[6] and Institute of Development, Aging and Cancer, Tohoku University, Seiryo-machi 4-1, Aoba-ku, Sendai 980-8575, Japan[7]

*To whom correspondence should be addressed. Tel. +81-22-717-8477. Fax. +81-22-717-8482.
Email: satake@idac.tohoku.ac.jp

Edited by Dr Toshihiko Shiroishi
(Received 9 May 2012; accepted 1 March 2013)

Abstract

The common marmoset is a new world monkey, which has become a valuable experimental animal for biomedical research. This study developed cDNA libraries for the common marmoset from five different tissues. A total of 290 426 high-quality EST sequences were obtained, where 251 587 sequences (86.5%) had homology ($1E^{-100}$) with the Refseqs of six different primate species, including human and marmoset. In parallel, 270 673 sequences (93.2%) were aligned to the human genome. When 247 090 sequences were assembled into 17 232 contigs, most of the sequences (218 857 or 15 089 contigs) were located in exonic regions, indicating that these genes are expressed in human and marmoset. The other 5578 sequences (or 808 contigs) mapping to the human genome were not located in exonic regions, suggesting that they are not expressed in human. Furthermore, a different set of 118 potential coding sequences were not similar to any Refseqs in any species, and, thus, may represent unknown genes. The cDNA libraries developed in this study are available through RIKEN Bio Resource Center. A Web server for the marmoset cDNAs is available at http://marmoset.nig.ac.jp/index.html, where each marmoset EST sequence has been annotated by reference to the human genome. These new libraries will be a useful genetic resource to facilitate research in the common marmoset.

Key words: common marmoset; cDNA; gene resource

1. Introduction

The mouse is a widely used and well-studied model animal for biomedical research. Many techniques for sophisticated genetic manipulations to model diseases have been established and researchers hope that the results obtained can be extrapolated to humans. Although this assumption is true in some cases, there are several areas of biomedical research

† Present address: National Institute of Genetics, Yata 1111, Mishima 411-8540, Japan.
‡ Present address: Research Equipment Center, Hamamatsu University School of Medicine, Handayama 1-20-1, Higashi-ku, Hamamatsu 431-3192, Japan.
¶ Present address: Division of Cancer Genomics, National Cancer Center Research Institute, Tsukiji 5-1-1, Chuo-ku, Tokyo 104-0045, Japan.
§ Present address: Toyohashi University of Technology, Hibarigaoka 1-1, Tenpaku-cho, Toyohashi 441-8580, Japan.

where this proves to be more difficult. These areas include neuroscience, behavioural research, toxicology, drug development, and infectious diseases.[1] To overcome these limitations, efforts have been made to carry out biomedical studies in non-human primate model organisms, as the latter are more closely related to humans.

One of these established non-human primate model organisms is *Callithrix jacchus* (common marmoset). The marmoset is a small new world monkey and offers many advantages as an experimental animal over other non-human primates. It is small in size, which makes it comparatively easy to handle. Furthermore, it has been bred in captivity and its progeny have been maintained for >30 years in laboratory environments. Also, it does not harbour or transmit hazardous infectious agents. Therefore, the common marmoset is increasingly used in biomedical research worldwide. For example, models of autoimmune diseases involving the central nervous system have been developed in the common marmoset and it has been used extensively as a primate model.[2–4] More recently, genetically modified common marmosets have been produced successfully and their transgenes have been transmitted through the germ line.[5] In the future, it would be very useful to develop transgenic marmosets as models of human diseases.

Intensive efforts have been made to develop research tools for using the common marmoset as an experimental animal. For instance, several lines of monoclonal antibodies have been prepared, which are directed against immunity-related antigens of the marmoset.[6–8] Many, but not all anti-human antigen antibodies cross-reacted with the corresponding marmoset antigens, so it was necessary to establish marmoset-specific antibodies.[9] A pilot gene analysis study reported cDNA sequencing of immunity-related genes.[10] Based on genome-wide analyses, a draft sequence of the common marmoset, known as caljac3, was produced and made available to the public via the genome browser of the University of California Santa Cruz (http://genome.ucsc.edu/).

The current study describes the preparation of cDNA libraries for the common marmoset using five different cell types/tissues, which resulted in the identification of 290 426 high-quality EST sequences. These sequences were characterized by comparison with the sequences of six primate species, including humans. Overall, the EST sequences transcribed in the marmoset shared many common features with those from humans, whereas a small fraction was found to be unique to the marmoset.

2. Materials and methods

2.1. *RNA extraction and library construction*

Cytoplasmic RNA was extracted from the liver (MLI), brain and spinal cord (MSC), spleen (MSP), testis (MTE), and embryonic stem (ES) cells (MES) of the common marmoset using Trizol reagent. Marmoset ES cells were cultured as described previously.[11] Full-length cDNA libraries were constructed from the total RNAs of the aforementioned tissues/cells using a vector-capping method.[12] cDNAs generated from MLI, MSC, MSP, MTE, and MES were ligated into pGCAP1, pGCAPzf3, pGCAPzf3, pGCAP10, and pGCAP10 vectors, respectively. Colonies of *Escherichia coli* transformants were picked randomly, inoculated into 384-well plates using a Flexys colony picker (Genomic Solutions Ltd., Cambridgeshire, UK), and stored at −80°C.

2.2. *EST sequencing*

Colonies were picked from 99 plates for MSC; 200 plates each for MES, MSP, and MTE; and 201 plates for MLI (Supplementary Table S1). Sequencing templates were prepared using a TempliPhi DNA Amplification Kit (GE Healthcare UK Ltd., Buckinghamshire, UK). The sequencing reactions for the 5′-end directional ESTs were conducted using a BigDye Terminator v3.1 Cycle Sequencing Kit (Applied Biosystems, Inc., CA, USA). The sequence primers used for pGCAP1, pGCAP10, and pGCAPzf3 were 5′-AGGCCTGTACGGAAGTGT-3′, 5′-AGG CCTGTACGGAAGTGT-3′, and 5′-CAAGGCGATTAAGTT GGGT-3′, respectively. The sequencing reaction products were purified by ethanol precipitation and loaded onto 3730 DNA Analyzers (Applied Biosystems Inc.).

2.3. *Selection of high-quality EST data*

The raw sequence data were basecalled using the KB basecaller program, which identified 345 600 sequences. A cross-match program was applied to the raw data to remove sequences derived from vectors and those added as caps during plasmid construction (−minimach 10, −minscore 20). Low-quality sequences [quality value (QV) = one for each nucleotide ± 3 neighbouring nucleotides measuring <105 in length] were masked by *N* (average QV > 15). If *N* was longer than 10 nucleotides, sequences located 3′ of these *N* were removed. Finally, only high-quality sequences longer than 100 nucleotides were selected and used in further analyses (see the high quality column, Supplementary Table S1). There were 290 426 high-quality ESTs, which represented 84% of the raw sequence data. High-quality EST sequences were obtained frequently and were relatively abundant (93%) in MES and

MTE, whereas their frequencies were comparatively low (72–80%) in MLI, MSC, and MSP.

The sequence length was higher in MES and MTE (702–706 nucleotides), than in MLI, MSC, and MSP (514–551 nucleotides; see the length column in Supplementary Table S1). The differences in the average length of readable sequences and the differences in the frequency of high-quality ESTs probably reflected the quality of each cDNA library. The cDNA libraries were also evaluated for transcription initiation sites by searching for the presence or absence of cap structure-derived guanine nucleotides at the extreme 5′ end of each EST (see the G-cap column, Supplementary Table S1). The frequency of G-cap-positive sequences was >80% in all five cDNA libraries, indicating that the synthesis of most cDNAs was initiated at the 5′ end.

2.4. *Registration of the sequences*

All of the EST sequences were deposited in the DNA Databank of Japan. Their accession numbers are as follows; HX373156 to HX444163 for MES cDNAs, HX444164 to HX500395 for MLI cDNAs, HX500396 to HX529651 for MSC cDNAs, HX529652 to HX591448 for MSP cDNAs, and HX591449 to HX663542 for MTE cDNAs.

2.5. *Tools used for sequence analyses*

The following tools were used for sequence analysis: BLAST (The Basic Local Alignment Search Tool) finds regions of local similarity between sequences. The program compares nucleotide or protein sequences to sequence databases and calculates the statistical significance of matches),[13] BLAT (The BLAST-Like Alignment Tool uses the index to find regions in the genome likely to be homologous to the query sequence),[14] CD-HIT (a widely used program for clustering and comparing protein or nucleotide sequences. CD-HIT helps to significantly reduce the computational and manual efforts in many sequence analysis tasks and aids in understanding the data structure and correct the bias within a dataset),[15] CAP3 (a DNA sequence assembly program),[16] cross_match (this tool uses cross_match to mask vector/adapter sequences and optimally trim vector sequence and/or polyA/T trail. It takes a set of sequences to be masked, and a set of vectors/adapters used to perform masking),[17] EMBOSS (getorf finds and extracts open reading frames),[18] and InterProScan (a protein domains identifier).[19]

3. Results and discussion

3.1. *EST clustering and assembly*

The 290 426 sequences obtained by normalization of ESTs as in Section 2.3 were clustered and/or assembled to estimate how many genes/transcriptional units were read as ESTs (Table 1). Overlapping sequences were clustered within the longest sequence using the CD-HIT program, whereas overlapping sequences were assembled and extended into a contig using the CAP3 program. According to the CD-HIT program, the number of clusters varied from 10 010 in MLI to 29 028 in MTE. The summed number of contigs and singletons ranged from 8831 in MLI to 25 909 in MTE. According to both programs, MTE had the highest number of clusters/assemblies, suggesting that the testis had the greatest number of expressed transcriptional units. Notably, there were some more clusters than assemblies in each cDNA library. In fact, the total and non-redundant numbers in the five different libraries were 62 210 clusters and 60 568 assemblies (Table 1). This small difference (62 210 versus 60 568) suggests that most of the EST sequences obtained correspond to the mRNA 5′ end (as for another indication of similar performance of CD-HIT and CAP3, see Supplementary Fig. S1).

3.2. *Assignment of marmoset ESTs to the Refseq mRNAs of primates*

All 290 426 sequences were examined by comparing them with the known sequences registered at the NCBI as Refseq mRNAs (http://ncbi.nlm.nih.gov/RefSeq/). Refseqs from six different primates were used in the reference dataset, including *Homo sapiens*, *Pan troglodytes*, *Pongo abelii*, *Macaca mulatta*, *Nomascus leucogenys*, and *C. jacchus*. It should be noted that the human Refseqs were based on cDNA

Table 1. Clustering of ESTs by CD-HIT and assembly of ESTs by CAP3

Libraries	Number of ESTs	Number of clusters by CD-HIT	Number of contigs and singlets assembled by CAP3
MES	71 009	17 467	15 837 = 5519 (contig) + 10 318 (singlet)
MLI	56 232	10 010	8831 = 3319 (contig) + 5512 (singlet)
MSC	29 258	12 309	10 617 = 3764 (contig) + 6853 (singlet)
MSP	61 831	16 600	14 268 = 5086 (contig) + 9182 (singlet)
MTE	72 096	29 028	25 909 = 8044 (contig) + 17 865 (singlet)
All	290 426	62 210	60 568 = 17 232 (contig) + 43 336 (singlet)

Parameters used in CD-HIT and CAP3 programs were default.

sequences, whereas the Refseqs from other primate species were based mainly on the predictions of genomic sequences. The search program used was BLASTn and the threshold of significant homology was set to $1E^{-100}$, which was a very strict criterion.

A total of 239 920 and 231 084 sequences shared homology with human and marmoset Refseqs, respectively (Table 2). Homology with the combined Refseqs from the six primates was found for 251 587 sequences (85.6% of 290 426). Therefore, these 251 587 sequences were designated as primate homologues. The average length of the homologous sequences was 528 nucleotides. Of these 251 587 sequences, 4974 sequences were identical to their corresponding Refseq sequences, whereas 94 102 sequences shared 100% nucleotide sequence identity only with the aligned homologous regions. Additionally, 931 sequences shared homology with the Refseqs of non-primates. Most of these sequences were homologous to mouse Refseqs, suggesting that they were probably derived from mouse cells that were used as a feeder layer to culture ES cells.

Out of the above described 251 587 primate homologues, only sequences that shared homology with the Refseqs of all six primates were extracted, and that yielded 199 511 sequences. Then, for each of 199 511 sequences, the alignments between the EST and Refseq with the highest score among the six primates were selected, and 199 511 sequences were grouped into six for each primate species. Finally, the average identities and coverage were calculated using the alignments for each primate species (Table 3). As expected, the highest sequence identity (99%) was between the marmoset EST and marmoset Refseq. The average sequence identities between the marmoset EST and the Refseqs of the other five primate species were in a similar range (94–95%). Thus, the sequences differed by ~5% between the marmoset and the other five primates. The coverage was highest between the marmoset EST and human Refseq (91%), whereas it was lowest between the marmoset EST and marmoset Refseq (84%). This difference of 6% corresponded to 25 nucleotides, so it is likely that the alignment of the EST and marmoset Refseqs started 25 nucleotides downstream from the 5′ end of the marmoset Refseq. This might suggest that the 5′UTR of the marmoset Refseq was not predicted precisely from its genomic sequence.

In the above assignment of marmoset ESTs to primates' Refseqs in Table 2, the Refseqs used as references can be re-classified into non-overlapping, distinct gene entities. Homologous sequences of 239 920 and 231 084 corresponded to 13 825 human and 13 499 marmoset genes, respectively (see the numbers in parenthesis in Table 2). In addition, we searched for HomoloGenes (http://www.ncbi.nlm.nih.gov/homologene) that are found in common among *Homo sapiens*, *Pan troglodytes*, and *Macaca mulatta*, and detected 9879 Homologenes. When identities and coverage between marmoset ESTs and primates' Refseq were recalculated for these 9879 Homologenes (see the numbers in parenthesis in Table 3), coverage increased by 2–3%, whereas identity between marmoset and human remained the same (94–95%). Thus, it appears again plausible that the sequences diverge by 5% between marmoset and other primates including human.

3.3. *Mapping marmoset ESTs to the human genome*

Each marmoset EST sequence (total 290 426 reads) was mapped to the human genome (hg19)

Table 2. Assignment of common marmoset ESTs to primates' Refseq

Species derivation of Refseq	Number of ESTs homologous to Refseq (number of homologous genes)
Homo sapiens	239 920 (13 825)
Pan troglodytes	233 913 (14 372)
Callithrix jacchus	231 084 (13 499)
Pongo abelii	231 354 (13 898)
Macaca mulatta	229 151 (13 677)
Nomascus leucogenys	228 749 (13 296)
Six primates	251 587
Non-primates	931

EST sequences of common marmoset (total 290 426) were referred to primates' Refseq mRNA that are registered at NCBI. Homology was searched using BLASTn and judged significant at $<1E^{-100}$.

Table 3. Identity and coverage between homologous marmoset ESTs and primates' Refseq

Species derivation of Refseq	Identity for Refseq (for 9879 HomoloGenes)	Coverage for Refseq (for 9879 HomoloGenes)
Homo sapiens	94.88% (94.54%)	91.14% (93.91%)
Pan troglodytes	94.86% (94.54%)	88.84% (92.11%)
Callithrix jacchus	99.55%	84.70%
Pongo abelii	94.77%	87.36%
Macaca mulatta	94.73% (94.44%)	87.20% (89.66%)
Nomascus leucogenys	94.72%	87.80%

Identity (%) represents a degree of identity between the aligned two sequences of high-scoring segment pairs, whereas coverage (%) represents a ratio of aligned sequence length over an entire length of EST. See the text as for the details how identity and coverage were calculated.